

Supplementary Information

Accompanying manuscript ‘Multiple sulfur isotopic reservoirs in the Moon and implications for the evolution of planetary interiors’

Samples

Representing all six Apollo landing sites, the fifteen Apollo thin section samples studied here were supplied by NASA’s Curation and Analysis Planning Team for Extraterrestrial Materials (CAPTEM). The samples are polished rock thin-sections of ~30 µm thickness. A diverse selection of lunar basalts, including low-Ti mare basalts (pigeonite basalts, olivine basalts and gabbroic basalts) and high-Al mare basalts with a range of crystallisation ages from ~3.1 Ga to ~3.9 Ga, and a KREEP-rich basalt (15386) were used in this study. With the exception of sample 14053, all of the mare basalts are pristine with no signs of alteration from secondary processes such as metamorphism or impact shock. In addition, apatites in feldspathic granulitic impactite (79215) and feldspathic polymict breccia (67915) were analysed in this study to perform inter-laboratory comparisons with the existing published data¹⁷ and to check mass balance calculations with $\delta^{34}\text{S}$ values known for trolite¹⁵, respectively. Furthermore, apatites in a lunar meteorite, Sayh al Uhaymir (SaU) 169, a hot desert ‘find’ from Oman, were analysed as proof of concept for the adapted nano-scale secondary ion mass spectrometry (NanoSIMS) S isotope protocol.

Ilmenite basalt: 10044,645

A high-Ti (low-K) coarse-grained porphyritic ilmenite basalt predominantly composed of pyroxene, plagioclase and ilmenite^{45,46}. The mesostasis of 10044 is composed of silica, troilite, Fe-metal, K-rich glass, tranquillityite (rare) and apatite⁴⁵. Symplectite is also observable within the mesostasis region. The apatite grains in 10044,645 are commonly subhedral to anhedral (Supplementary Figure 1) and can vary considerably in size from <10 µm to >~200 µm in the longest dimension.

Pigeonite Basalt: 12031,7

As coarse-grained basalt, 12031 is predominantly composed of large pyroxene and plagioclase grains (up to 3 mm and 3.5 mm in the longest dimension, respectively)⁴⁷⁻⁵⁰. Contrasting gabbroic and graphic textures are seen within the specific sample 12031,7 (the same section is studied here) involving the juxtaposition of more granular textures against regular intergrowths of plagioclase and pyroxene⁴⁷. The mesostasis regions are very coarse grained and contain large apatite grains (~75 µm in the longest dimension) (Supplementary Figure 1). Apatites are rarely euhedral, with most being subhedral to anhedral and are found alongside large grains of troilite (some >100 µm in the longest direction), ilmenite and silica. Apatites are also found within non-mesostasis pyroxene grains, which suggests that

apatite was not solely an interstitial crystallising mineral. The symplectite in 12031,7, it is not directly associated with apatite.

Pigeonite Basalt: 12039,45

A microgabbro and a low-Ti mare basalt, 12039 is a coarse grained ophitic rock, predominantly composed of pyroxene and plagioclase. The acquisition of cathodoluminescence (CL) images of apatites in the specific sample studied here (12039,45) reveal notable concentric and oscillatory zoning within multiple grains. Apatites found within the mesostasis region are predominantly euhedral-basal with a few being subhedral crystals (Supplementary Figure 1). The grains occur as clusters, with sizes ranging from <20 µm up to ~60 µm in the longest dimension, that are surrounded by similarly sized potassium feldspar, troilite, tridymite and tranquillityite grains.

High-Al Basalt: 14053,19

An ophitic coarse-grained low-Ti basalt with ~50 vol.% of large pyroxene grains (up to 5 mm) alongside lesser quantities (~40 vol.%) of plagioclase grains (up to 2 mm)^{51,52}. Apollo sample 14053 is dubbed the most reduced rock from the Moon because mineral reduction reactions, such as the breakdown of fayalitic olivine and chromite-ulvöspinel, have been observed within the rock. As no impact-melt texture has been detected within the sample, the cause of the reduction is thought to have been due to subsequent solar wind (hydrogen) implantation to the exterior of the rock, post-crystallisation⁵¹. The apatite grains present within the studied sample (14053,19) are euhedral (sparse), subhedral and anhedral and are between 20 µm and 100 µm in the longest dimension (Supplementary Figure 1).

Olivine basalt: 15016,7

Sample 15016 is a low-Ti medium-grained, olivine-normative, vesicular basalt that contains large vesicles of 0.7–5 mm in diameter⁴⁵ that comprise ~60% of the rock. Many vesicles are thinly lined with black glass and ilmenite plates within their interior walls (Butler, 1971; ^{54,55}). Sample 15016 is porphyritic due to its large phenocrysts of pyroxene (1 – 2 mm) and olivine (0.8 – 1 mm). The plagioclase grains make up ~20–22 vol.% of the rock (^{45,51,55,56}). Mesostasis regions (~0.3 vol.%) contain troilite and traces of Fe-Ni metal inclusions⁴⁵ and, within the specific sample studied (15016,7), this is the region where apatite is predominantly found but it also occurs in non-mesostasis regions where it is surrounded by pyroxene and plagioclase. There are many small euhedral, basal sections of apatite as well as anhedral grains in 15016,7 with sizes ranging from <10 µm to ~40 µm in the longest dimension (Supplementary Figure 1). One apatite analysed with NanoSIMS was found to be zoned with respect to S and Cl (Supplementary Figure 2).

Pigeonite basalt: 15058,15

Sample 15058 is a coarse-grained, porphyritic basalt⁵³ with phenocrysts of clinopyroxene and laths of plagioclase⁵⁵. The specific sample studied (15058,15) has apatites that range from euhedral, to subhedral, to anhedral and some with a very thin and long straw-like appearance, the latter of which are predominantly found surrounded by pyroxene and potassium feldspar grains. Other apatites are immediately adjacent to silica, ilmenite, troilite and, occasionally, symplectite. Some apatite grains of <5 µm in size are found clustered together, making their boundaries harder to discern, whereas other straw-like apatite grains are up to 200 µm in the longest dimension (Supplementary Figure 1).

Gabbroic basalt: 15065,85

A coarse-grained, low-Ti mare basalt⁵⁷, sample 15065 is predominantly composed of zoned clinopyroxenes and plagioclase (^{53,55}). The whole rock has two distinct regions: one of mafic and one of felsic composition⁵³ which is possibly due to magma chamber zoning or contamination from non-gabbroic material⁵⁸. The specific sample studied (15065,85) has apatites included within pyroxene grains and also in contact with plagioclase, potassium feldspar, ilmenite, tridymite and troilite. Apatites frequently exist in tight clusters (<2 µm – ~80 µm in the longest dimension) and are euhedral to anhedral. Fewer larger apatite grains, up to 200 µm in the longest dimension, are found as very fine laths that cross-cut pyroxene (Supplementary Figure 1). Apatite zonation is detectable when analysed with cathodoluminescence but not seen in backscatter electron images. Like 15016, one apatite analysed with NanoSIMS was found to be zoned with respect to S and Cl (Supplementary Figure 2).

Pigeonite Basalt: 15085,15

Sample 15085 is a coarse-grained, low-Ti basalt which contains vugs of a few milimeters in size that represent ~3–5 vol.% of the rock⁵⁹. As a quartz-normative basalt that lacks olivine, 15085 is predominantly composed of very large pyroxene and plagioclase grains (up to 10 mm in the longest dimension)⁵⁵. Apatites are located within both the mesostasis regions of the sample studied (15085,15) alongside large troilite grains (often up to ~50 µm), ilmentite, silica, potassium feldspar and symplectite, and away from mesostasis regions where they are enclosed in pyroxene grains. Sample 15085 contains the largest apatite analysed in the mare basalts of this study: ~200 µm in longest dimension, but there are also much smaller grains of ~10 µm. Apatites vary in shape from small euhedral to (predominantly) anhedral and lath-shaped (Supplementary Figure 1).

KREEP basalt: 15386,46

Potassium, rare earth element, phosphorous (KREEP) basalt 15386 is a non-mare basalt sample that has incompatible trace element enrichment of 100 to 150 times that of chondritic (primitive) meteorite

compositions (e.g. ref. ⁶⁰). It is subophitic, pristine volcanic basalt that is predominantly composed of plagioclase and interstitial pyroxene. The mesostasis in the specific sample studied (15386,46) includes potassium feldspar, tranquillityite, baddeleyite, apatite, merrillite, ilmenite, plagioclase and silica. Exclusively found in mesostasis pockets, the apatite is between ~25 µm and ~250 µm in the longest dimension and varies from subhedral to anhedral or appears as long, straw-shaped grains (Supplementary Figure 1).

Porphyritic Pigeonite Basalt: 15475,17 and 15475,127

Described as a coarse-grained (porphyritic), low-Ti, quartz-normative mare basalt, 15475 contains 2–20 vol.% vuggy pore space and is visibly fractured at the scale of the thin sections⁵³. Pyroxene represents ~64–74 vol.% of the sample^{53,56} with large grains of up to 15 mm⁶². Mesostasis regions represent ~1 vol.% of the sample and are exclusively where apatite grains in the specific samples studied (15475,17 and 15475,127) are situated. The mesostasis regions contain silica, ilmenite, potassium feldspar, troilite, plagioclase and pyroxene. Potassium feldspar commonly appears as inclusions within apatite grains. The apatites are mostly euhedral to subhedral and are some of the largest observed in the samples studied (second to apatites of 15085,15) being ~50 µm to ~100 µm in the longest dimension (Supplementary Figure 1).

Olivine normative basalt: 15545,7

Sample 15545 is described as a porphyritic olivine mare basalt with late-stage interstitial plagioclase⁵³. The major constituents are pyroxene, plagioclase and olivine. Mesostasis regions are scattered throughout the thin section sample studied in this project (15545,7) and are where all of the analysed apatites are located. The typical mesostasis regions include potassium feldspar, ilmenite, troilite, Fe-Ni metal, olivine and pyroxene (Supplementary Figure 1). The majority of apatites (typically <10 µm to ~30 µm) are anhedral and contain inclusions of potassium feldspar or are surrounded by intricate lace patterns of potassium feldspar.

Olivine normative basalt: 15555,991

Sample 15555 is a large coarse-grained (porphyritic), vuggy, low-Ti olivine-normative basalt⁵⁶. The major constituents are pyroxene, plagioclase and olivine (e.g. refs. ^{45,54,56,61}). The apatite grains of the specific sample studied (15555,991) are predominantly located within the mesostasis regions (0.2-5 vol.%) alongside troilite, potassium feldspar, silica and ilmenite but apatite is also found enclosed within Fe-rich pyroxene grains, often with plagioclase inclusions. Typically, the apatite grains are between <5 µm and ~40 µm in the longest dimension (Supplementary Figure 1) and appear as clusters of small euhedral or larger anhedral grains. Apatite grains with long, thin straw-like appearances (up to ~100 µm

in the longest dimension) that give the impression of having been splashed into the rock, are also common.

Vesicular olivine normative basalt: 15556,137

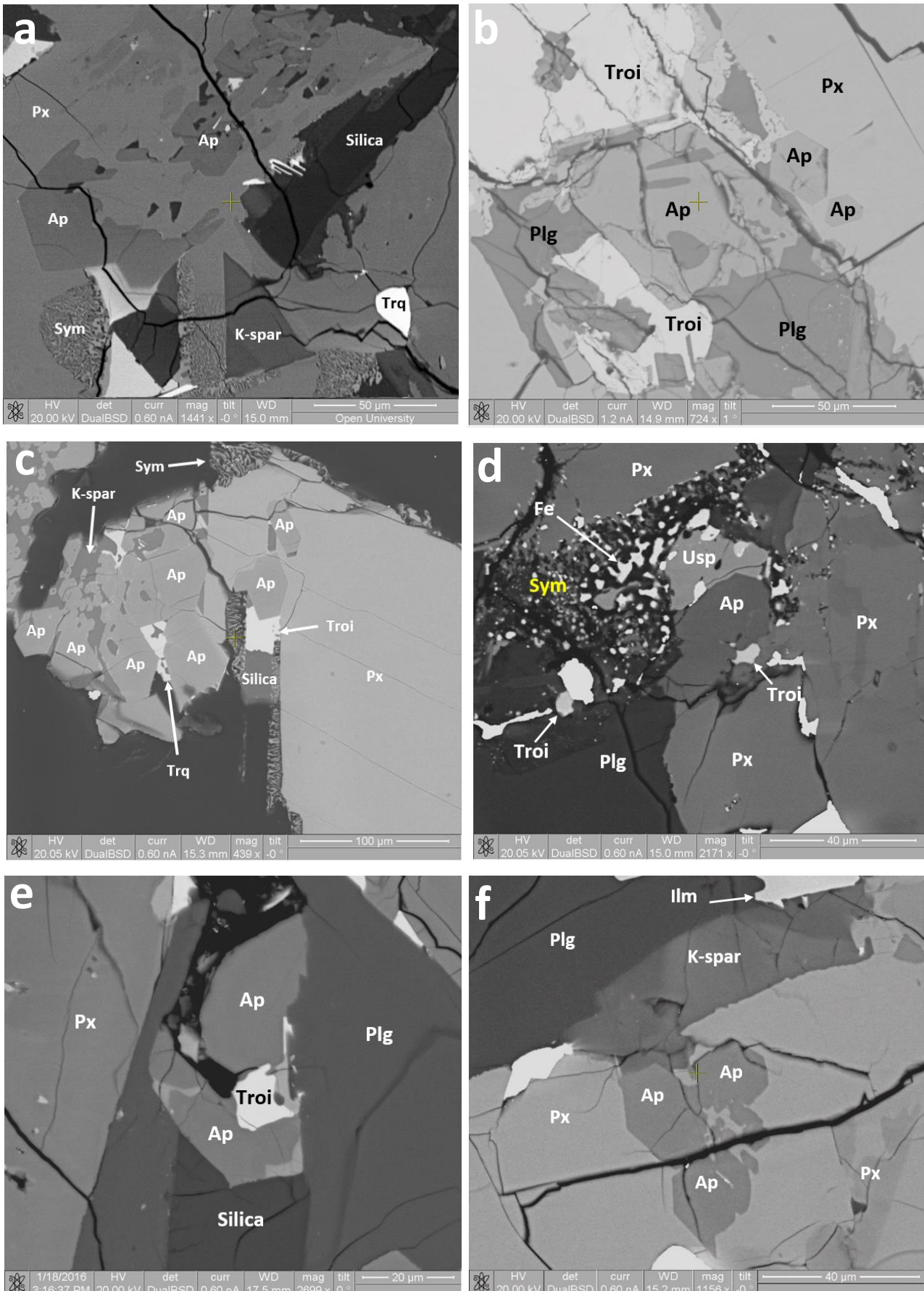
Sample 15556 is a fine-grained, low-Ti mare basalt. It is highly vesicular with ~50 vol.% of the rock containing vesicles of up to ~5 mm that are often lined with opaque minerals (e.g. ilmenite) or glass⁴⁵. Olivine phenocrysts (~0.1 –0.4 mm) comprise ~5 vol.% of the sample and appear to be less abundant and smaller in regions of the rock where there are more vesicles⁶². Approximately 50 vol.% of the sample is composed of pyroxene phenocrysts⁵³. The matrix of the rock contains granular pyroxene and tabular-shaped plagioclase along with glass and opaque minerals of ilmenite, ulvöspinel and chromite between the larger silicate grains^{45,56}. The mesostasis regions of the specific sample studied (15556,137) typically contain ilmenite, troilite, silica, potassium feldspar, plagioclase and pyroxene (Supplementary Figure 1). A sample of very few apatites that are all located in mesostasis regions, the grains are anhedral or straw-like and relatively small with sizes ranging from <5 µm to ~30 µm in the longest dimension.

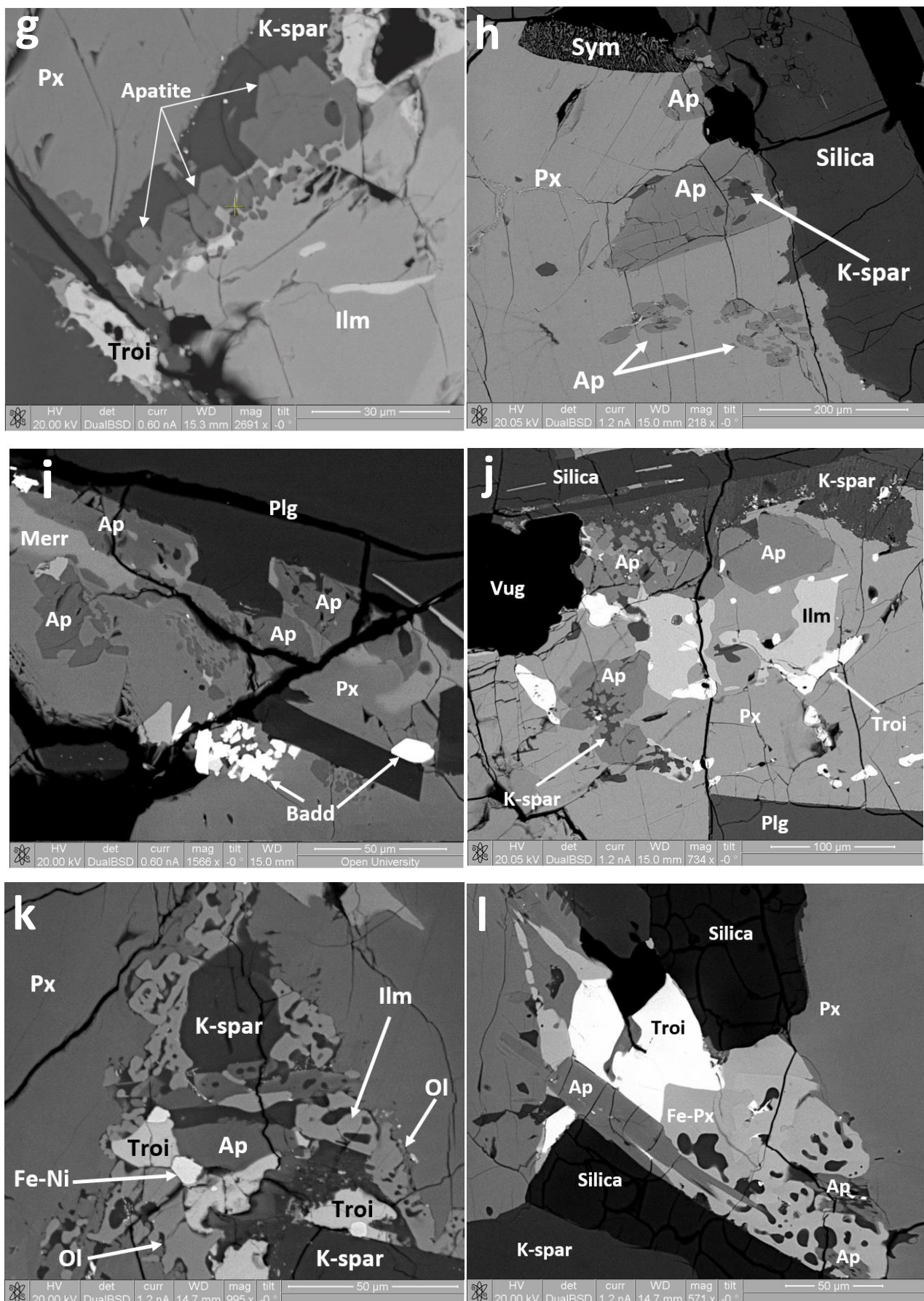
Feldspathic polymict breccia: 67915,75

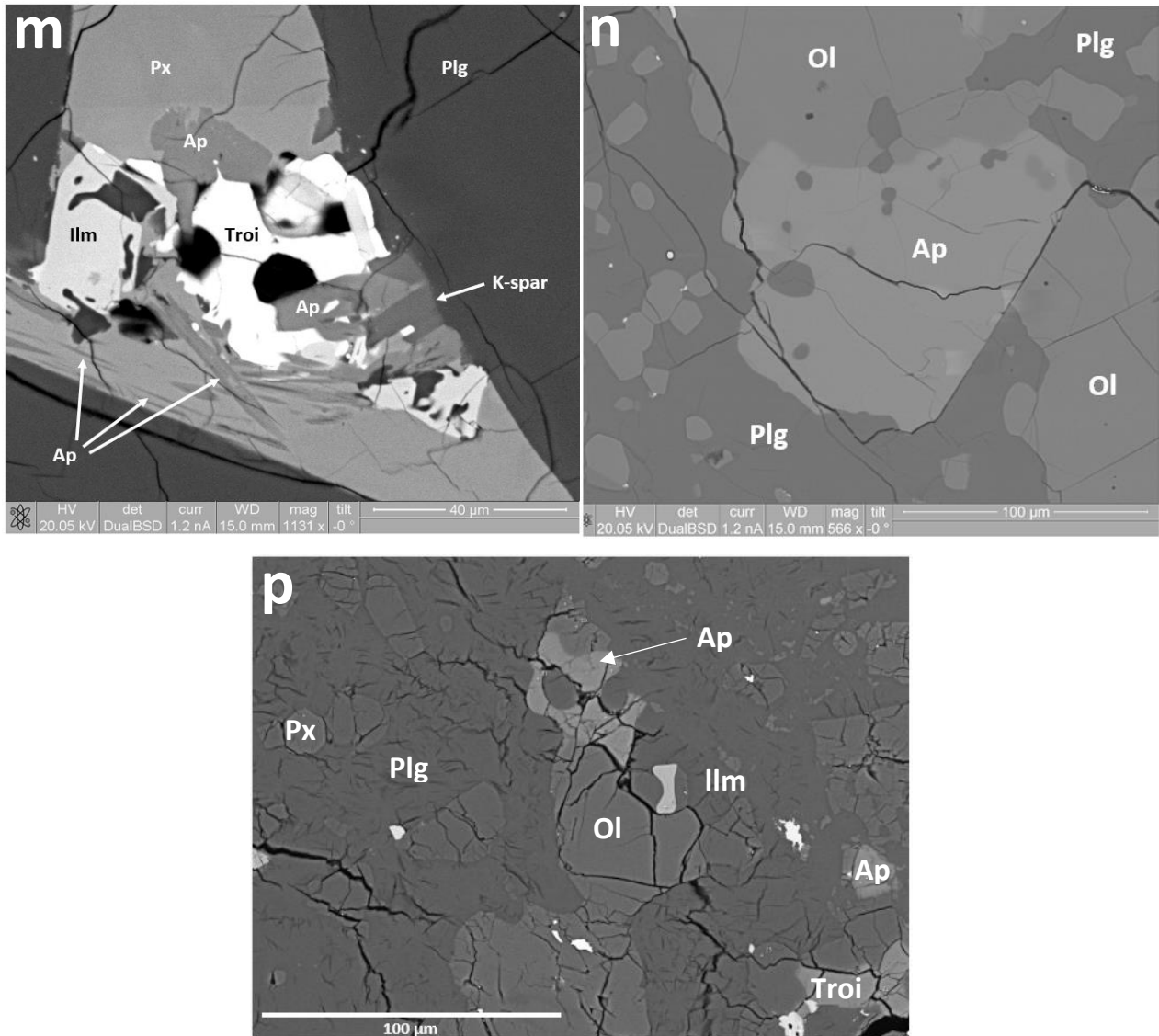
Composed of two main polymict lithologies, 67915 is a heavily shocked rock containing many large clasts of anorthosite, ferrogabbro and troctolite. The specific sample studied (67915,75) is dominated by plagioclase and has lesser quantities of olivine and pyroxene (Supplementary Figure 1). Apatites are found within small mesostasis regions which typically feature ilmenite, troilite and olivine grains, all surrounded by a plagioclase matrix. The apatites are predominantly anhedral (Supplementary Figure 1) and contain many fractures. For the most part, the grains are small (<10 µm), but narrow apatites of up to ~60 µm in the longest dimension also exist in the studied sample.

Feldspathic granulitic impactite: 79215,50

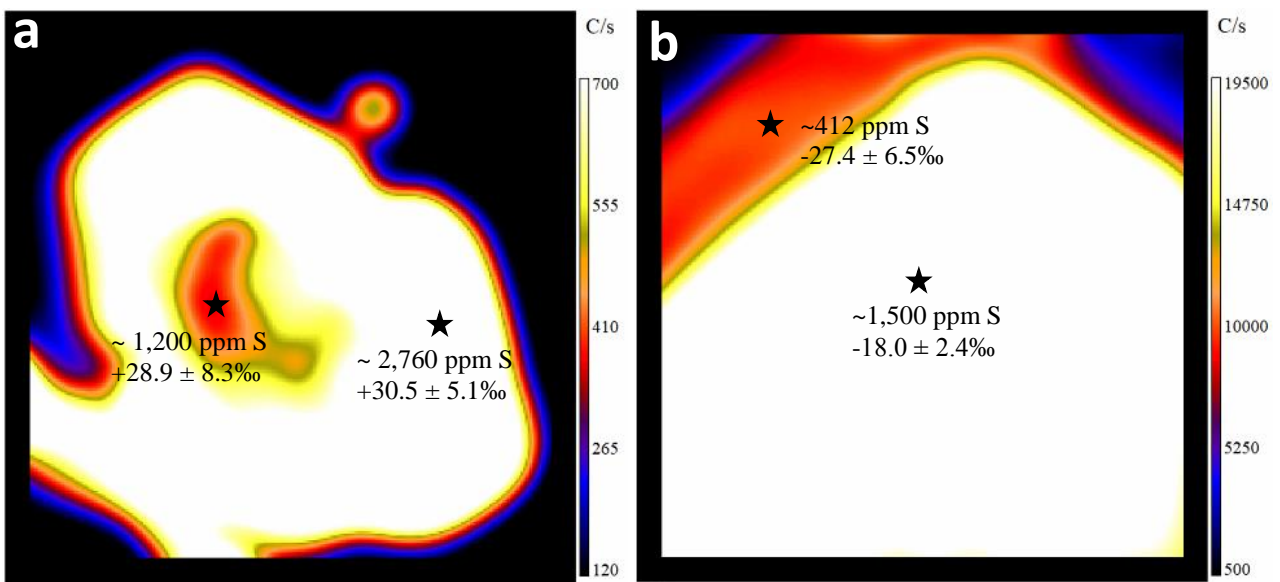
A KREEP-poor sample, 79215 is a holocrystalline, feldspar-rich rock that consists of both relict lithic and single mineral clasts that intermingle with a crushed, mixed and annealed granoblastic matrix. The matrix accounts for ~72% of the rock which was formed by prolonged annealing, crushing and limited mixing of clasts of anorthite plagioclase, olivine, orthopyroxene, clinopyroxene and small quantities of spinel, ilmenite, metal and troilite^{63,64}. The remaining ~28% of the rock is composed of mafic, anorthositic and mineral clasts⁶⁴. For the specific sample studied (79215,50), apatite exists as large (up to ~500 µm in the longest dimension) subhedral to anhedral grains (Supplementary Figure 1), located almost exclusively outside of the main matrix area. The apatites are predominantly found as megacryst clasts (smaller ones are ~10 µm) and are believed to have formed during the annealing process because they are observed to enclose some of the matrix material such as plagioclase and olivine^{17,54}.







Supplementary Figure 1. Backscatter electron (BSE) images of the apatite grains analysed in this study and their surrounding petrographic context. **a**, 10044,645 (image courtesy of Jessica Barnes, The Open University); **b**, 12031,7; **c**, 12039,45; **d**, 14053,19; **e**, 15016,7; **f**, 15058,15; **g**, 15065,85; **h**, 15085,15; **i**, 15386,46; **j**, 15475,17; **k**, 15545,7; **l**, 15555,991; **m**, 15556,137; **n**, 79215,50; **p**, 67915,75. Where the mineral abbreviations are: Ap = apatite, Badd = baddeleyite, Fe = iron, Fe-Ni = iron-nickel, IIm = Ilmenite, K-spar = potassium feldspar, Merr = merrillite, Ol = olivine, Plg = plagioclase, Px = pyroxene, Sym = symplectite, Troi = troilite, Trq = tranquillityite, Usp = Ulvöspinel.



Supplementary Figure 2. Secondary ion images of zoned apatites acquired with NanoSIMS. **a**, Apollo sample 15016, apatite grain Ap42 showing clear zonation with respect to S. **b**, Apollo sample 15065, apatite grain Ap005b, with sharp boundary zonation with respect to S. Where C/s is counts per second of ^{32}S and where a probe size of ~ 2 pA and ~ 25 pA was employed for 15016 and 15065, respectively.

Methods

Ion microprobe analysis

Image processing

Each ion imaging analysis performed with Cameca NanoSIMS 50L typically consisted of between 50 and 500 frames (dependent upon the S or Cl abundances within the sample) which were stitched together and processed using the L'image software (Larry Nittler, Carnegie Institution of Washington) to form one image. All images were corrected for detector dead time and aligned for possible stage shifts. Typically, homogeneous ROIs selected for an apatite standard were $\sim 7 \mu\text{m} \times 7 \mu\text{m}$. For the samples, only regions with little, to negligible, variation were isolated and used for data processing, with heterogeneous regions such as hotspots of S and cracks or apatite grain boundaries excluded.

X-ray absorption near-edge structure spectroscopy

For the May 2019 analytical session, fresh thin section samples prepared by NASA's Curation and Analysis Planning Team for Extraterrestrial Materials (CAPTEM) were used to ensure that samples had not previously been exposed to other X-ray measurement techniques (e.g. EPMA or XANES) that might have caused prior beam damage. The X-ray beam was defocussed to give a larger beam size of $\sim 20 \times 20 \mu\text{m}$, which required apatite grains to be larger than those analysed in the January session and meant that only Apollo samples containing apatites of $>\sim 50 \mu\text{m}$ in the longest dimension

were included for S-XANES analysis. Compared with the January analytical session, the S-XANES spectra collection range was 2450 eV – 2550 eV with steps of 0.5 eV and 1 s per energy point. The larger apatite grains analysed in May have relatively low S abundances when compared with those analysed in January and, with the above instrument setup, little to no S signal reached the detector. Phosphorous swamped the low S signals. In order to increase the S signal, the beam size was reduced to ~ $>10 \times 10 \mu\text{m}$ and to maintain a low P signal, the Kapton tape was increased to ~25 μm and the detector was positioned further away from the sample during analysis. This improved the S signal, but only very low levels of S were detected.

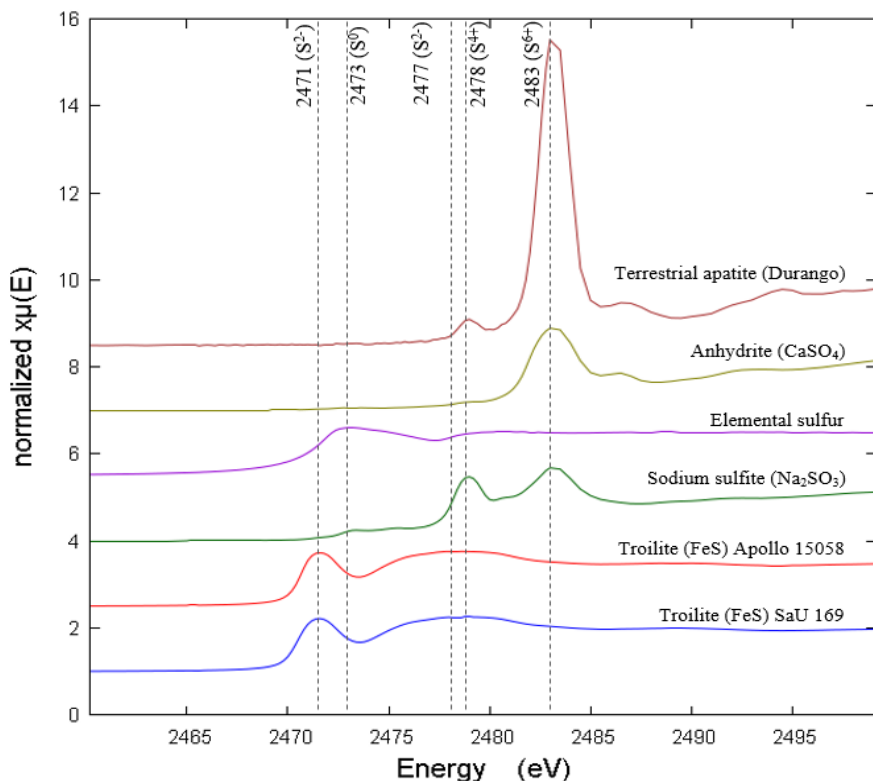
Peak area integration analysis, background removal and S peak area ratio

The raw S spectra were edge-step normalized in the X-ray absorption spectroscopy (XAS) data processing software Athena⁶⁵. Normalization involved regressing a line both to the pre-edge and to the post edge region of a spectrum and extrapolating both lines back to the absorption edge of the spectrum. The pre-edge line was subtracted from the post-edge line at the point where both lines passed through E0 to give the ‘edge-step’ parameter. The subtracted data was divided by the edge-step value which flattened the pre- and post-edge regions and assigned values of 0 and 1, respectively. Supplementary Table 1 shows the reference materials used in this study and Supplementary Figure 3 shows the normalized S-XANES spectra of those materials used to define the peak energy positions of S oxidation states (S^{6+} , S^{4+} and S^{2-}) that could exist in apatite. Anhydrite and terrestrial apatite (Durango) define the S^{6+} peak at an energy of ~2483 eV. The Durango also has another peak at ~2478 eV which is thought to represent the presence of S^{4+} and, therefore, multiple S oxidation states in terrestrial apatite (e.g. ref. ⁴¹). Troilite (FeS) from two different lunar samples (Apollo 15058 and lunar meteorite SaU 169) show a sharp peak at ~2471 eV that represents S^{2-} . It is reported that a broad peak also exists for S^{2-} at ~2476.8 eV (e.g. ref. ⁶⁶), therefore, both the sharp and the broad peaks (~2477 eV in Supplementary Figure 3) were used in this study to identify S^{2-} in lunar apatite samples. Sodium sulfite appears to have two prominent peaks in Supplementary Figure 3, with one at ~2478 eV and the other at ~2483 eV. Whilst anhydrous (used in this study) is more stable than hydrous sodium sulfite, it can become oxidized to sodium sulfate if it is not kept completely dry and it is likely that the second peak (~2483 eV) represents partial oxidation⁶⁶. Therefore, only the first peak (~2478 eV) was used to identify S^{4+} in lunar apatites in this study. The energy peak for elemental sulfur (S^0) is positioned at ~2473 eV.

Supplementary Table 1. Reference standard material used for S-XANES spectroscopy.

Reference standard	Known sulfur oxidation state*	Location/ source
Troilite (FeS)	2-	Contained within Apollo sample 15058 and lunar meteorite SaU 169.
Elemental S	0	Supplied by I18 beamline scientist.
Sodium-sulfite (Na_2SO_3) (anhydrous)	4+	Purchased from Fisher Scientific.
Terrestrial apatite (Durango)	6+	Durango, Mexico. Supplied by Excalibur Mineral Corp, USA.
Rose gypsum (anhydrite: CaSO_4)	6+	Courtesy of Peter Landsberg, The Open University

* refs.^{41,66} and European Synchrotron Radiation Facility (ESRF).

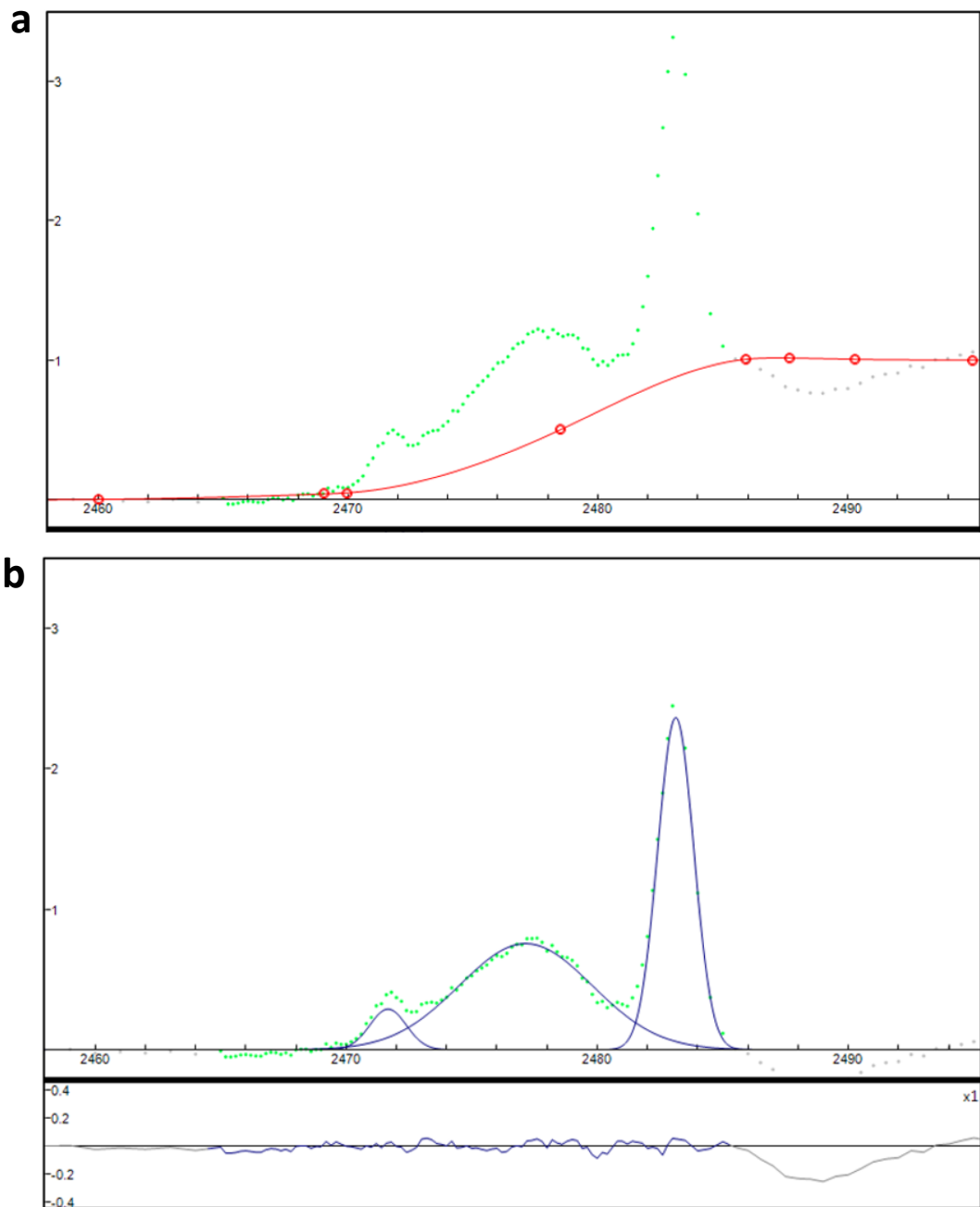


Supplementary Figure 3. Edge-step normalized XANES spectra at the S K-edge of S reference materials. Individual spectra are offset vertically for clarity.

The normalized data was exported from Athena and loaded into the non-linear curve fitting software Fityk (version 1.3.1)⁶⁷ to perform peak area integration analysis. The background signal of each S-XANES spectrum was removed, using a similar method to Konecke et al.⁴¹, with an exponentially modified Gaussian (EMG) function in Fityk. For all spectra, the pre- and post-edges of the EMG function were set to 0 and 1, respectively, with the EMG function inflection point set to ~2479 eV

(Supplementary Figure 4). The peak fitting method with background removal is reported to be a semi-quantitative method, whereby the derived peak area ratios are proportional to the abundance of each S oxidation state in an apatite grain⁴¹.

With use of the known peak energy positions of S⁶⁺ (~2483 eV), S⁴⁺ (~2478 eV) and S²⁻ (~2471 eV and ~2477), individual Gaussian curves were positioned onto the background-subtracted S-XANES spectrum in Fityk so that the highest point (the peak) of the Gaussian curve was positioned at a known absorption energy. Peak fitting of each spectrum was performed with the Gaussian area (Gaussian-A) function in Fityk. The peak area fitting energy range was truncated so that only S-XANES data between ~2465 eV and ~2485 eV (the S K-edge) were included within the peak fitting (Supplementary Figure 4).



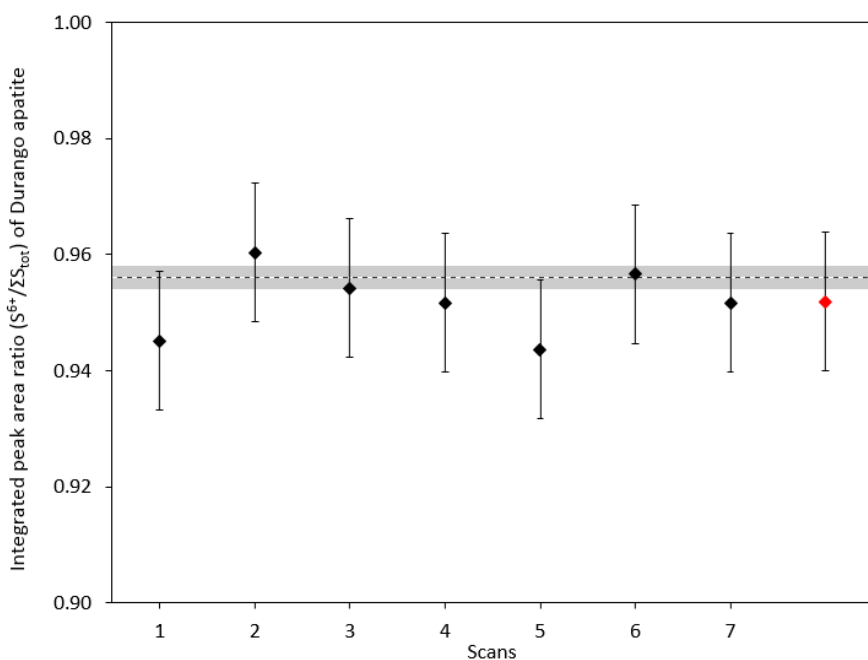
Supplementary Figure 4. An example of background removal and peak fitting of S-XANES in Fityk. The normalized S-XANES spectrum of data collected from a single point on an apatite within Apollo sample 15065 is shown in **a**, where the green dotted line is the spectrum and the red line is the EMG function (fitted background) before subtraction. The y-axis is the absorption intensity. Visible grey dots represent data that was excluded from the fit (in the pre- and post-edge regions). **b**, The same spectrum is shown but the background has been subtracted and the Gaussian-A functions (added peaks, in blue) have been fitted. The lower panel of **b**, shows the peak fitting residual, which represents the difference between the best-fitting model and the data points, and is based on weighted sum of squared residuals (WSSR) (chi-square)⁶⁷.

The peak fitting process determined the individual area values of peaks representing S^{6+} , S^{4+} and S^{2-} (where present) and the corresponding residual standard deviation for all of the fitted spectra. To calculate the S^{6+} content of a lunar apatite sample, the peak area value of S^{6+} was divided by the sum

of the peak area values of all sulfur (e.g. $S^{6+} + S^{4+} + S^{2-}$) to give a peak area ratio of ‘ S^{6+} to total sulfur’: $S^{6+}/\Sigma S_{\text{tot}}$.

Reproducibility

In order to confirm the reproducibility of the S-XANES measurements (and the data reduction technique), repeated S-XANES measurements were made of the Durango apatite (Supplementary Figure 5) which resulted in an average integrated $S^{6+}/\Sigma S_{\text{tot}}$ peak area ratio of 0.95 ± 0.01 (2σ standard deviation). An average integrated $S^{6+}/\Sigma S_{\text{tot}}$ peak area ratio of Durango apatite has been previously reported by⁴¹ as 0.956 ± 0.002 (2σ) based on an average of twenty S-XANES scans. Supplementary Figure 5 shows that, within error, the measurements performed were also accurate based on the external average value reported by⁴¹.



Supplementary Figure 5. The precision and accuracy of S-XANES analyses. Individual S-XANES data collection scans of Durango apatite are plotted as the integrated peak area ratios ($S^{6+}/\Sigma S_{\text{tot}}$) (black diamonds). The dashed line at 0.956 represents the average $S^{6+}/\Sigma S_{\text{tot}}$ ($n = 20$) of Durango apatite, derived independently⁴¹, where the grey band denotes the reported 2σ uncertainty (0.002). The red diamond represents the average of the measurements ($n = 7$) made in this study, where $S^{6+}/\Sigma S_{\text{tot}} = 0.95 \pm 0.01$ (2σ). The error bars associated with each of the measurement points represent the residual standard deviation (c.f. Supplementary Figure 4).

Results and discussion

NanoSIMS

The NanoSIMS results for both S and Cl abundances and isotopes are presented in Supplementary Table 2.

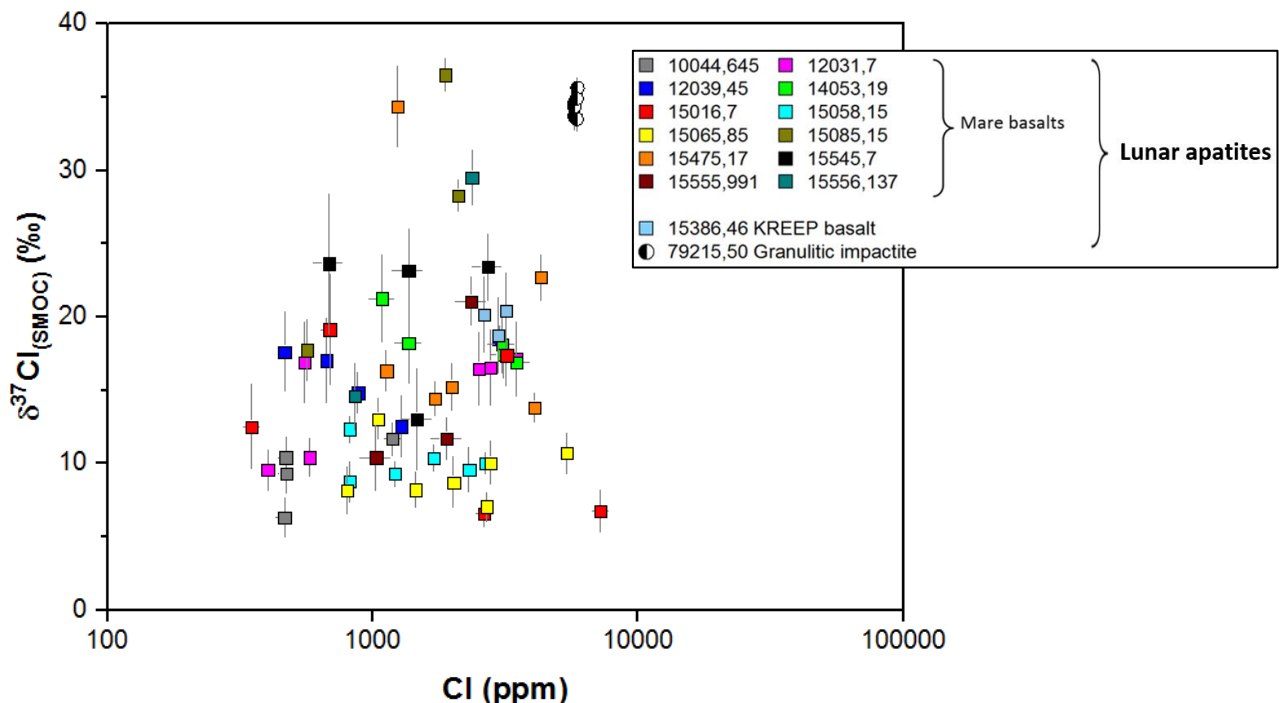
Chlorine

Overall, the range of Cl abundance for apatites of twelve different Apollo mare basalt samples (excluding KREEP-rich basalt 15386 and granulitic impactite 79215) studied here is ~6,900 ppm, with a minimum and maximum value of ~350 ppm and ~7,230 ppm, respectively. The isotope range ($\delta^{37}\text{Cl}(\text{SMOC})$) for the samples is ~30‰, with a minimum and maximum Cl isotope value of +6.5‰ ± 0.9‰ (2 σ) and +36.5‰ ± 1.1‰ (2 σ), respectively (Supplementary Table 2). The apatites of 15386 have $\delta^{37}\text{Cl}$ values of +18.7 ± 2.6‰ to +20.4 ± 2.6‰ and Cl abundance of ~2,600 ppm and ~3,200 ppm. The apatites of 79215 have much higher $\delta^{37}\text{Cl}$ and Cl abundances compared with all of the other samples, with minimum and maximum $\delta^{37}\text{Cl}$ of +33.5 ± 0.8‰ and +35.6 ± 0.8‰, respectively and minimum and maximum Cl abundances of ~5,750 ppm and ~5,900 ppm, respectively.

Chlorine measurements of apatites in five Apollo low-Ti mare basalt samples not previously reported in the scientific literature (12031, 15085, 15475, 15545 and 15556) are presented for the first time in this study. Both the chlorine isotope and abundance results are very spread out and scattered across the graph in Supplementary Figure 6. Individual apatites from 15085, 15475 and 15556 have $\delta^{37}\text{Cl}$ values of >~+23‰, which appear to be much higher than the majority of other apatite data points shown on the graph. Three apatite grains in sample 15085 have a $\delta^{37}\text{Cl}$ range from +17.1 ± 2.1‰ up to the highest $\delta^{37}\text{Cl}$ value recorded for all of the lunar samples, +36.5 ± 1.1‰. The minimum and maximum abundances are ~560 ppm and ~2,100 ppm Cl, respectively. Apatites in sample 15475 have a very high $\delta^{37}\text{Cl}$ value of +34.4 ± 2.7‰ but also a much lower value of +13.8 ± 1.0‰ with a similarly large range of abundances from ~4,100 ppm Cl down to ~1,130 ppm Cl. Only two apatite grains were measurable for Cl within sample 15556 giving a $\delta^{37}\text{Cl}$ of +14.6 ± 2.2‰ and +29.5 ± 1.9‰ and corresponding abundances of ~850 ppm and ~2,400 ppm Cl. The apatites within all three of these mare basalts samples show heterogeneity with respect to both Cl abundance and $\delta^{37}\text{Cl}$.

The other two newly analysed samples display less variation in $\delta^{37}\text{Cl}$ values but are still heterogeneous with respect to Cl abundance. Spanning six apatite grains, sample 12031 has $\delta^{37}\text{Cl}$ values from +9.6 ± 1.4‰ to +17.1 ± 2.5‰ and a large spread in abundance from ~400 ppm to ~3490 ppm Cl. Sample 15545 has three apatite grains with very uniform values of +23.7 ± 4.8‰, +23.1 ± 2.9‰ and +23.4 ± 2.3‰ and corresponding Cl abundances of ~680 ppm, ~1,360 ppm and ~2,700

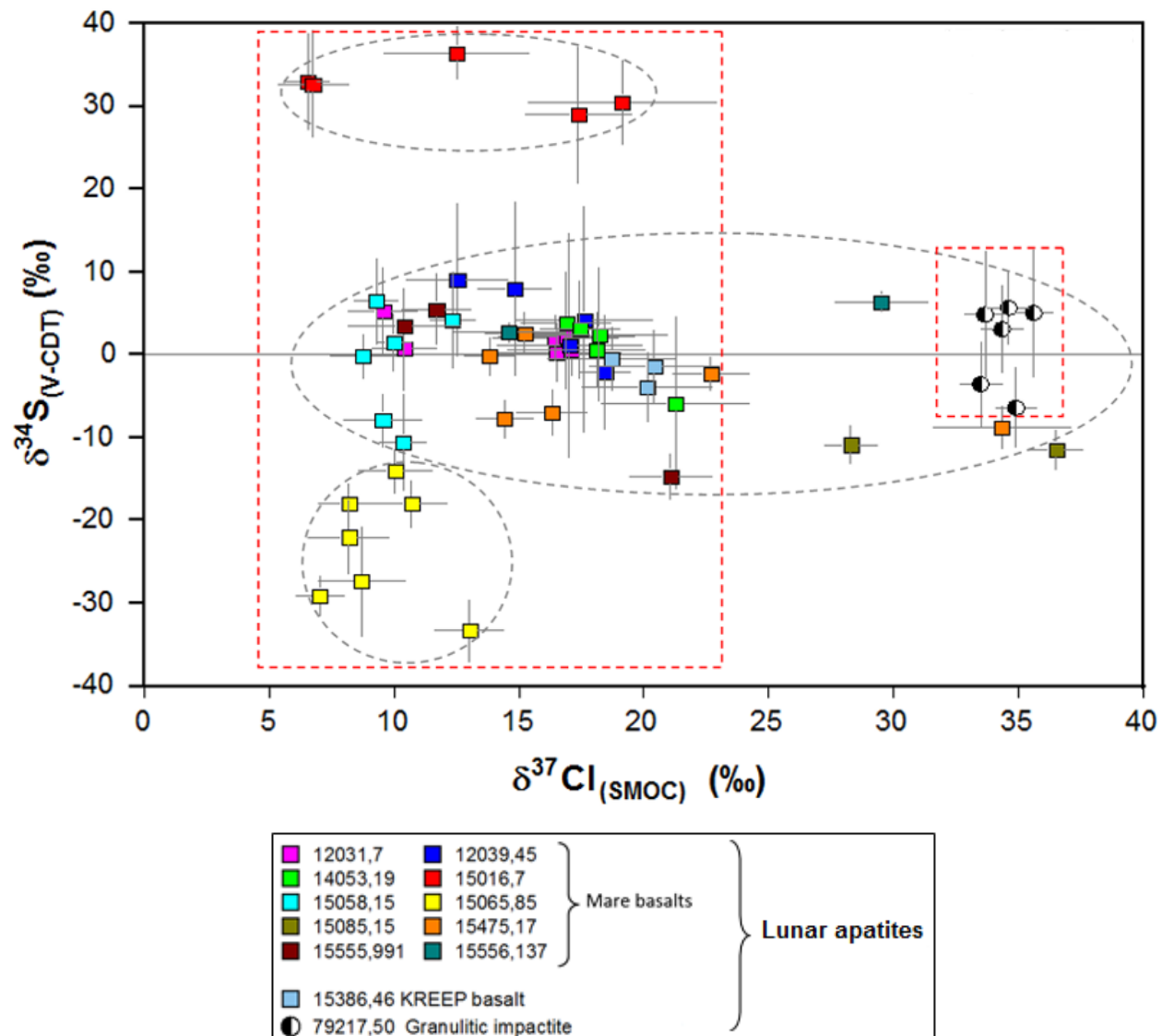
ppm, respectively. The fourth grain has similar Cl contents (~1,465 ppm) but a lower $\delta^{37}\text{Cl}$ value of $+13.0 \pm 3.4\text{\textperthousand}$. No systematic correlation is discernible between Cl abundance and the corresponding Cl isotope values and, unlike the S results, no notable clusters of the data are apparent.



Supplementary Figure 6. Plot of Cl isotopes ($\delta^{37}\text{Cl}_{(\text{SMOC})}$) against Cl abundance (ppm) in apatite for the analysed lunar samples. The results of Cl measurements performed with NanoSIMS for apatites of twelve Apollo mare basalts, a KREEP basalt and a granulitic impactite are shown. Note the log scale on the x-axis. The error bars are at the 2σ uncertainty associated with the measurements.

What is clear from the $\delta^{37}\text{Cl}$ and Cl abundance reported here for the five samples is that there is considerable heterogeneity. The inter-sample heterogeneity in Cl isotopic composition in lunar apatite might be reflecting the effects of magma degassing (preferential loss of ^{35}Cl) during mare volcanism (e.g. ref. ²⁷) and/ or interactions between mare magmas, derived from isotopically light and Cl-poor mantle source regions, with differing quantities of the Cl-rich and isotopically heavy urKREEP/KREEP component (e.g. refs. ^{25,26}). The observed intra-sample variations in isotopic compositions might have been caused by a combination of relatively local events such as late-stage magma degassing and/ or variable interactions with a Cl-rich metasomatic agent, such as a vapour phase (e.g. refs. ^{17,68}). Crystallisation of apatites potentially occurred both before and after vapour phase interactions resulting in heterogeneous $\delta^{37}\text{Cl}$ values and Cl abundances (e.g. ref. ⁶⁸).

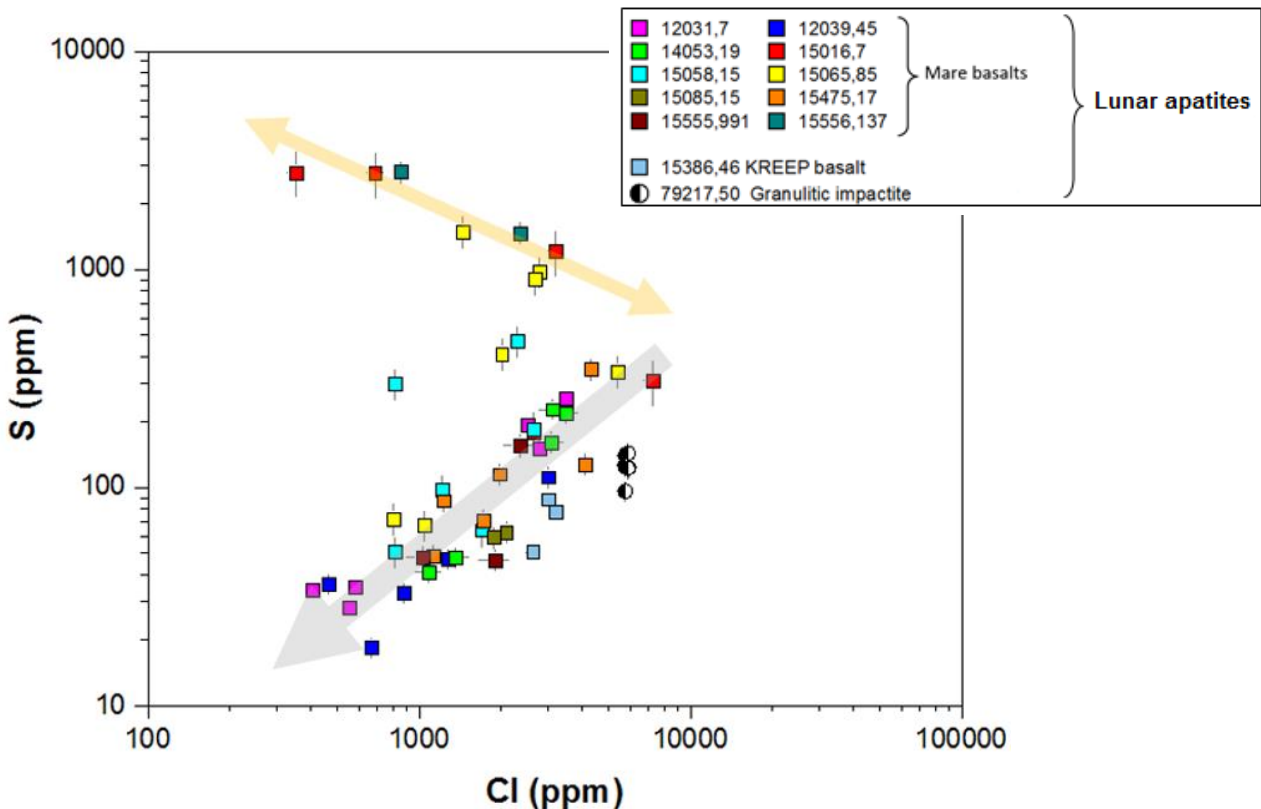
Sulfur and chlorine compared



Supplementary Figure 7. Plot of S isotopes ($\delta^{34}\text{S}(\text{V-CDT})$) against Cl isotopes ($\delta^{37}\text{S}(\text{SMOC})$) in apatite for the analysed lunar samples. There is an absence of relationship between S and Cl for apatites of ten Apollo mare basalts, a KREEP basalt and a granulitic impactite. The three distinct isotope clusters of S (grey dashed ovals) and the largely separated chlorine isotope groups of the mare basalts and the granulitic impactite sample (the larger and smaller red dashed rectangles, respectively) are discernible. The vertical and horizontal error bars are the 2σ uncertainty associated with the measurements. See main article for further details regarding this figure.

From the measurement of S and Cl, this study demonstrates that there is no overall significant statistical correlation between S and Cl abundance ($R^2 = 0.03$) in apatites of the twelve samples shown in Supplementary Figure 8. However, there are two apparent *trends*. For apatites containing relatively high S abundances ($>\sim 450$ ppm), degassing of S and Cl is unlikely to have been the only process operating in the late-stage silicate melt. The negative trend, whereby S increases as Cl decreases and

vice-versa can be explained by a separate oscillatory process involving the loss of S and Cl from the melt by degassing on the one hand and, on the other, an increase of the S and Cl concentrations in the melt as crystallisation of the melt progressed. What is not clear is which of these two processes (loss through degassing or an increase through crystallisation) was dominant and what the impact/ extent of each process was on each element. For relatively low S abundances (~ 450 ppm) in apatite, a positive trend between S and Cl abundance suggests that simultaneous degassing of S and Cl from the late-stage silicate melt could have occurred.



Supplementary Figure 8. Plot of S abundance (ppm) against Cl abundance (ppm) for the measured apatites of ten Apollo mare basalts, a KREEP basalt and a granulitic impactite. There is no overall statistically significant correlation but a positive trend (grey arrow) and a negative trend (orange/yellow double-headed arrow) are apparent. See text for further details. The error bars are the 2σ uncertainty associated with the measurements. Note the log scale on both axes.

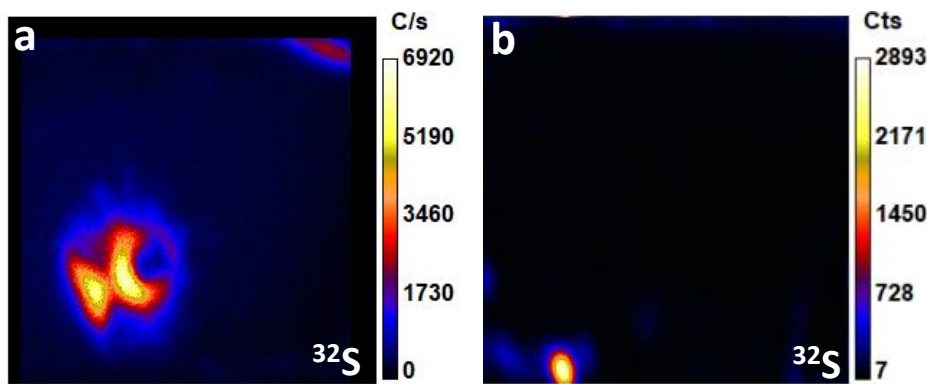
A comparison of sulfur abundance and isotopes in lunar apatite

Lunar sulfur abundances reported in the scientific literature are dominated by measurements of bulk-rock samples, lunar soils, volcanic glasses and melt inclusions. Mare basalt bulk-rocks contain ~ 550 – $2,770$ ppm S (e.g. refs. ^{6–9,13,14,69}), whereas lunar soils have up to ~ 830 ppm S (refs. ^{70,71}), volcanic glasses have ~ 110 – 580 ppm S (e.g. refs. ^{16,34}) and melt inclusions have ~ 360 – $1,900$ ppm S (e.g. refs. ^{72–75}). At the time of writing and to the best of our knowledge, only three published studies^{17,76,77} have

measured S abundance in lunar apatite with an ion microprobe, enabling a direct comparison with the measurements carried out in this project.

The S abundances of five individual apatite grains measured in high-Al basalt 14053 are much lower (~41–229 ppm S) (Supplementary Table 2) than that reported for a different thin section of the same sample⁷⁶, where seven analyses on a single apatite grain gave a range of ~310–460 ppm S. Likewise, a comparison of pigeonite basalt 12039 shows that the S abundance reported for a single apatite grain from a different thin section for the same sample⁷⁷ ranged from below the limit of detection to <~600 ppm S which, at the upper end, is far higher than the ~20–110 ppm S measured in this study. By contrast, the abundance of 102–111 ppm S reported¹⁷ for three different apatite grains from feldspathic granulitic impactite 79215 is similar to the ~96–144 ppm S determined by this study for six individual apatite grains in a different thin section from the same sample.

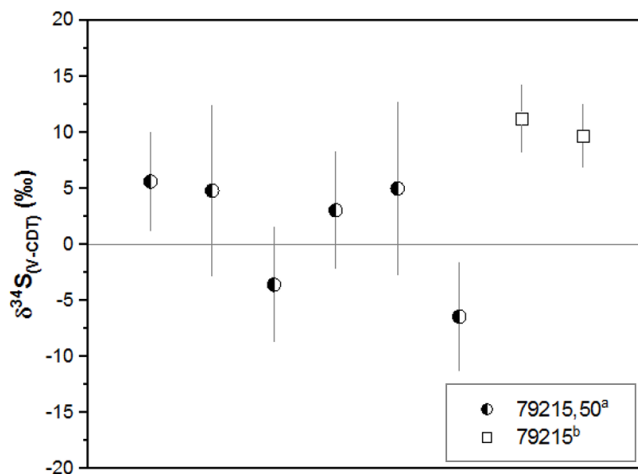
It is possible that the higher S abundances reported for 14053 (ref. ⁷⁶) and 12039 (ref. ⁷⁷), respectively, are due to the measurement of an apatite grain that is uncharacteristically S-rich. For example, it has been suggested that rims of apatites in 12039 are S- and Cl-rich, possibly due to interaction with a late-stage metasomatic S- and Cl-carrying vapour phase, transported from a deeper decompressing magma⁷⁸. Alternatively, the differences could be due to incorporation of S hotspots within the grains that would not be detected with prior investigative techniques (e.g. electron probe microanalysis or scanning electron microscopy) given their very small sizes (<<1 µm). Using the NanoSIMS imaging mode, sulfur hotspots were clearly observed in apatites of 12039 and 14053 (Supplementary Figure 9), but, importantly, not in 79215. The S hotspots contained far higher counts of S relative to the homogeneous apatite regions and could either be avoided during analysis or removed during image processing.



Supplementary Figure 9. Sulfur hotspots in lunar apatite. **a**, 10 x 10 µm NanoSIMS image of an apatite in Apollo sample 14053 is shown with a sulfur (³²S) hotspot just towards the bottom-left of centre with up to ~6,900 counts per second. **b**, An equivalent image for Apollo sample 12039 is shown with a sulfur hotspot at the bottom left of an apatite grain with up to ~2,800 counts per second.

Similarly to S abundance measurements of lunar materials, most of the S isotope studies in the scientific literature are dominated by measurements of lunar bulk-rock and soil samples (e.g. refs.^{6-14,70,71}). There have been a few *in situ* S isotope investigations of lunar volcanic glasses (e.g. ref.¹⁶) and, at the time of writing, the S isotope value of just a single lunar apatite grain in one rock sample has been published¹⁷.

The S isotope results of this study for six different lunar apatite grains of sample 79215 (Supplementary Table 2) are between $-6.4 \pm 4.9\text{‰}$ and $+5.6 \pm 4.4\text{‰}$ (2σ). Two measurements were made on a single apatite grain from a different thin section of the same sample¹⁷ which resulted in marginally higher values of $+11.3 \pm 3\text{‰}$ and $+9.7 \pm 2.8\text{‰}$ (2σ). Within statistical uncertainty, the results of this study and those of Treiman et al.¹⁷ are the same (Supplementary Figure 10) which confirms the reproducibility of the S isotope measurements between the different laboratories.



Supplementary Figure 10. Reproducibility of S isotope measurements. The graph compares the results of S isotope measurements ($\delta^{34}\text{S}(\text{V-CDT})$ (‰)) made on six individual apatite grains in Apollo sample 79215,50 for ^a this study and two measurement points made on a single apatite grain for ^b Treiman et al.¹⁷ (thin section 79215,51 or 79215,56). The vertical error bars are the 2σ uncertainty associated with the measurements.

Mass balance

Given the dominance of troilite (FeS) within mare basalts³, the more restricted S isotope values reported for bulk-rocks predominantly reflect the $\delta^{34}\text{S}$ value of troilite, which is masking the far greater $\delta^{34}\text{S}$ range measured *in situ* in the minor S constituent apatite phase. Unlike apatite which crystallises from the silicate melt, troilite precipitates from an immiscible sulfide melt that is segregated from the silicate melt ($\text{Fe}^{2+} + \text{S}^{2-} \leftrightarrow \text{FeS}_{(\text{liquid})}$) if the concentration of sulfide in the silicate melt exceeds the sulfur content at sulfide saturation (SCSS)⁷⁹. Mass balance calculations show that if bulk-rock $\delta^{34}\text{S}$ values of $\sim -1.6\text{‰}$ to $+0.5\text{‰}$ (refs. ¹¹⁻¹³) for the mare basalt samples are adopted and assuming that, firstly, 85-99% of the bulk-rock S is contained in troilite and, secondly, that troilite

has an approximate $\delta^{34}\text{S}$ value of -1‰ to -3‰ (ref. ¹⁵), the $\delta^{34}\text{S}$ values measured in apatite in this study (-33.3‰ to +36.4‰) do not make a significant impact on the S isotopic composition of the bulk-rock. Troilite would have crystallised from the sulfide melt, which is likely to have experienced limited S isotope fractionation during H_2S degassing (e.g. ref. ³⁶), unlike the late-stage silicate melt from which apatite crystallised.

S-XANES

Not all of the apatites analysed with NanoSIMS could be analysed with S-XANES due to the limited beam time available at the synchrotron facility, low levels of S, small grain sizes and the proximity of FeS to some of the apatites. The number of S-XANES scans carried out on each apatite grain varied depending on practical considerations such as the size of the apatites and the need to avoid cracks, if present.

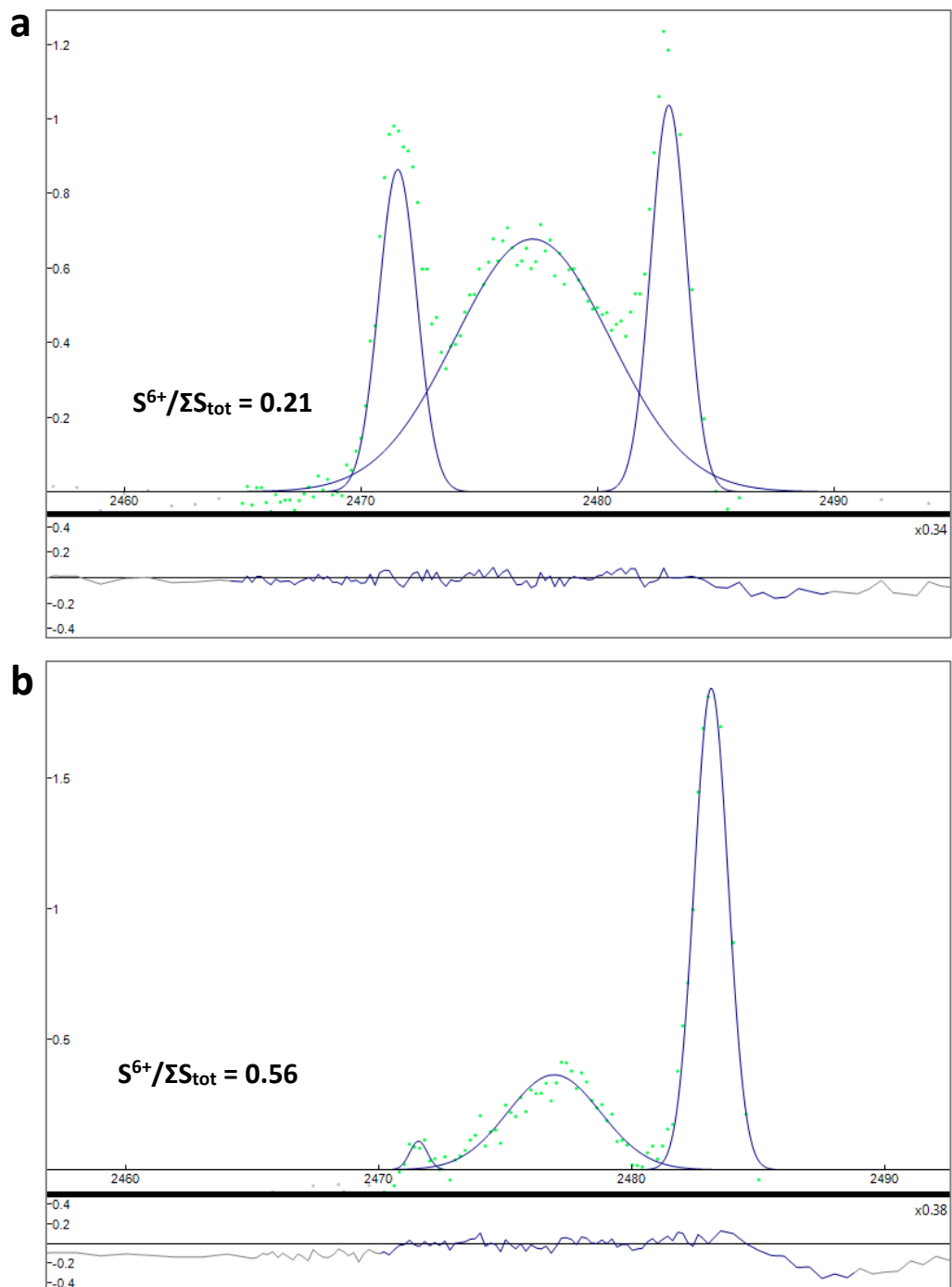
The individual S-XANES spectroscopy scan results for nine apatites in five different Apollo low-Ti mare basalt samples (12039, 15016, 15058, 15065 and 15475,127), lunar meteorite SaU 169, a terrestrial apatite (Durango) and non-apatite materials (pyroxene, symplectite glass and epoxy) of an Apollo sample are shown in Supplementary Table 3. A summary of the results is shown in Supplementary Table 4 which gives an average $\text{S}^{6+}/\Sigma\text{S}_{\text{tot}}$ value for the S-XANES scans of each analysed apatite. All of the apatite S-XANES spectra reported in this study have $\text{S}^{6+}/\Sigma\text{S}_{\text{tot}}$ ratios of >0, which means that the oxidation state of S in lunar apatite can provide an indication of the oxygen fugacity ($f\text{O}_2$) of a late-stage silicate melt and can, therefore, act as an oxybarometer (e.g. refs. ^{23,41}). Whilst S^{4+} was observed in the apatite of the Durango and lunar meteorite SaU 169, it was not detected in any apatites of the Apollo samples.

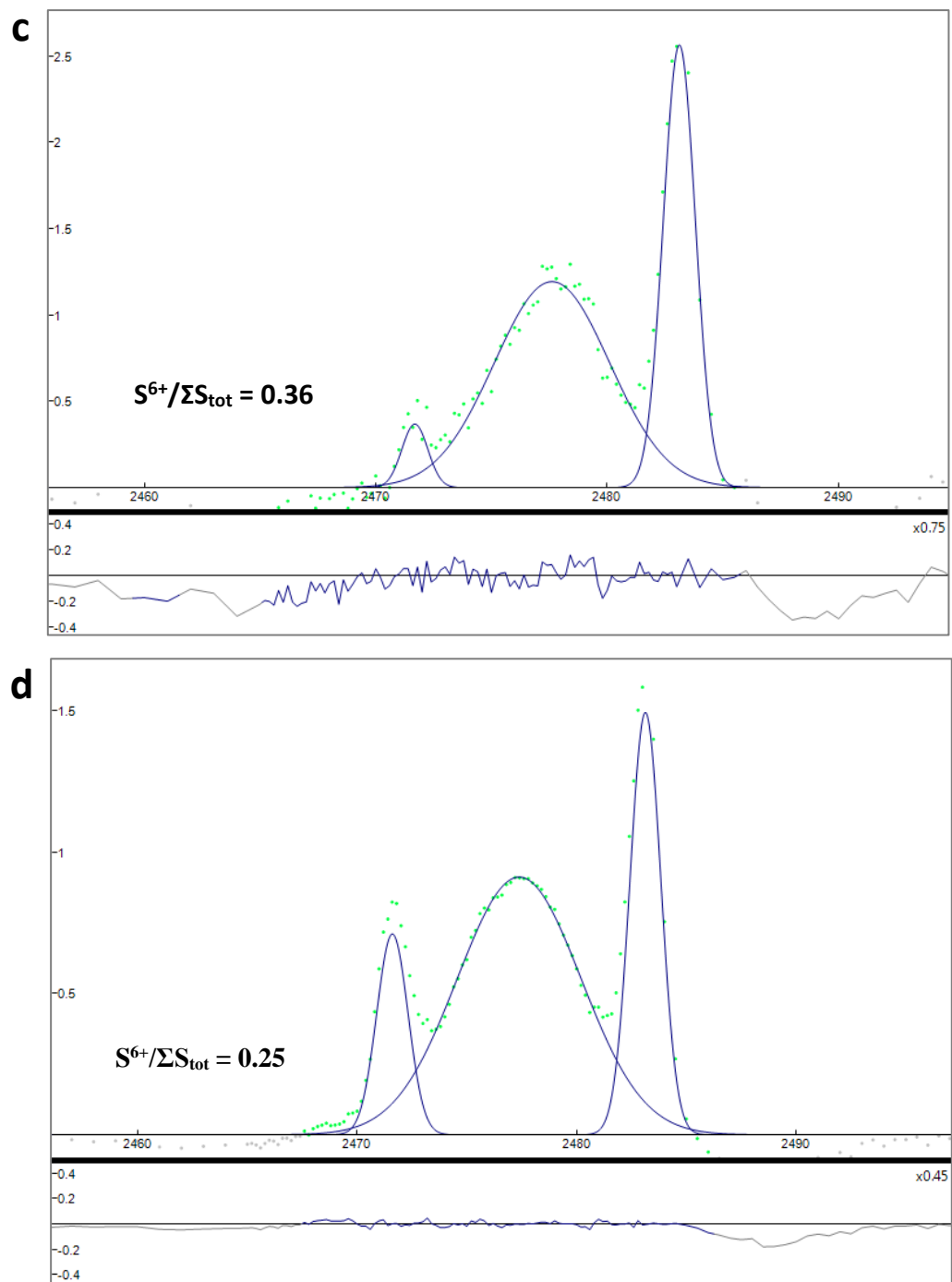
Supplementary Figure 11 shows a selection of the Fityk peak-fitted S-XANES spectra of apatite grains from the five Apollo samples. A combination of three absorption features, with variable intensities, related to S^{6+} (~2483 eV) and S^{2-} (sharp peak at ~2471 eV and broad peak at ~2476.8 eV) are apparent in the apatites. Additionally, S-XANES analyses of symplectite glass and pyroxene in close proximity to grain Ap012a of sample 15058 (Supplementary Tables 3 and 4 and Supplementary Figure 12) were carried out and show no spectral similarities with apatite Ap012a (Supplementary Figure 11). The epoxy of sample 15058 was also analysed but, because the S content was below the level of S-XANES detection, no S spectra could be acquired which suggests that S signals from the epoxy are unlikely to have affected apatite S-XANES measurements.

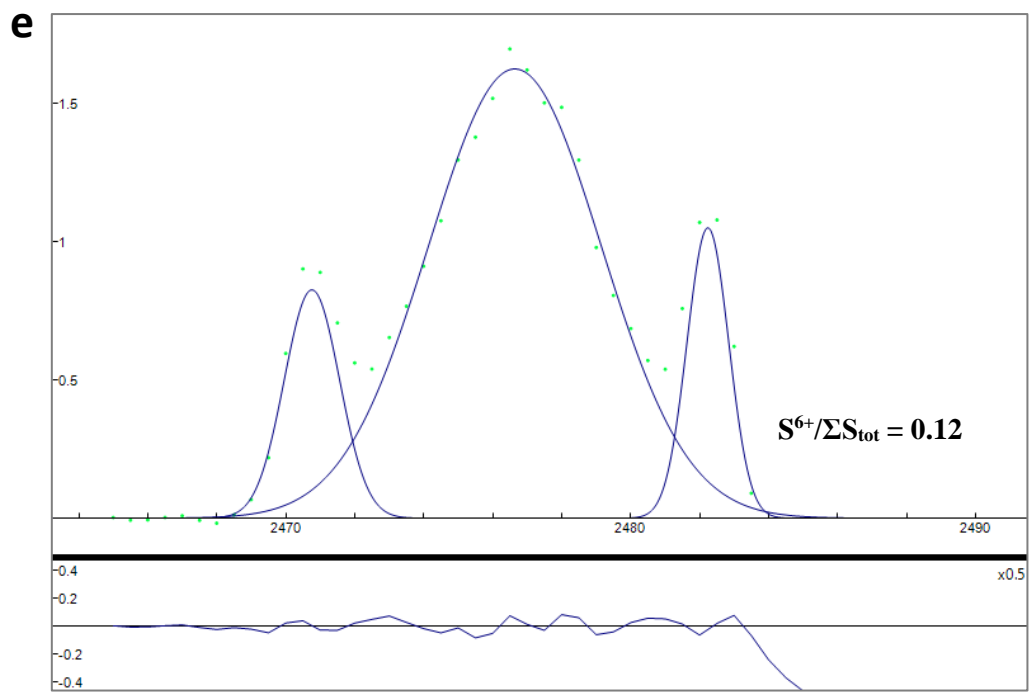
Supplementary Table 4. A summary of the S-XANES results. The average $S^{6+}/\Sigma S_{tot}$ ratio of the measurements made for individual apatite grains is recorded in the table. The corresponding S isotope values and S abundances determined in this study with NanoSIMS are also included. The individual S-XANES scan results are shown in Supplementary Table 3.

Session	Sample type	Sample I.D.	Analysis I.D.	Avg. $S^{6+}/\Sigma S_{tot}$	$\delta^{34}S$ (‰)	2σ (‰)	S (ppm)	2σ (ppm)
January 2019	Olivine basalt	15016,7	Ap42	0.55	29.7 *	6.7	1,987 *	464
	Gabbroic basalt	15065,85	Ap007 [†]	0.27	-29.1	2.4	903	146
			Ap005b	0.29	-22.7 *	4.5	957 *	155
			Ap001b	0.25	-18.0	2.8	341	55
			Ap003	0.36	-14.1	2.6	978	158
	Pigeonite basalt	15058,15	Ap012a	0.34	-7.9	3.2	472	76
			Ap016	0.30	-0.2	2.7	301	49
	Pigeonite basalt	12039,45	Ap001_a	0.23	9.0	9.2	47	5
			Ap001_f	0.39	-2.1	7.0	112	12
	Symplectite glass	15058,15	-	0.12	N/A	N/A	N/A	N/A
May 2019	Epoxy	15058,15	-	b.d.	N/A	N/A	N/A	N/A
	Pyroxene	15058,15	-	0.06	N/A	N/A	N/A	N/A
	Impact melt breccia (lunar meteorite)	SaU 169	SOI 7	0.86	1.4	4.2	245	19
			SOI 14	1.00	6.8	3.6	340	26
			SOI 15	1.00	29.9	3.5	477	37
	Terrestrial apatite	Durango	-	0.95	-	-	-	-
	Gabbroic basalt	15065,85	Ap007 [†]	0.19	-29.1	2.4	903	146
	Porphyritic pigeonite basalt	15475,127	Ap002	0.05	3.7	1.0	2332	227
			Ap003a	0.12	2.9	1.2	1329	130
			Ap003b	0.09	-1.2	1.3	646	63

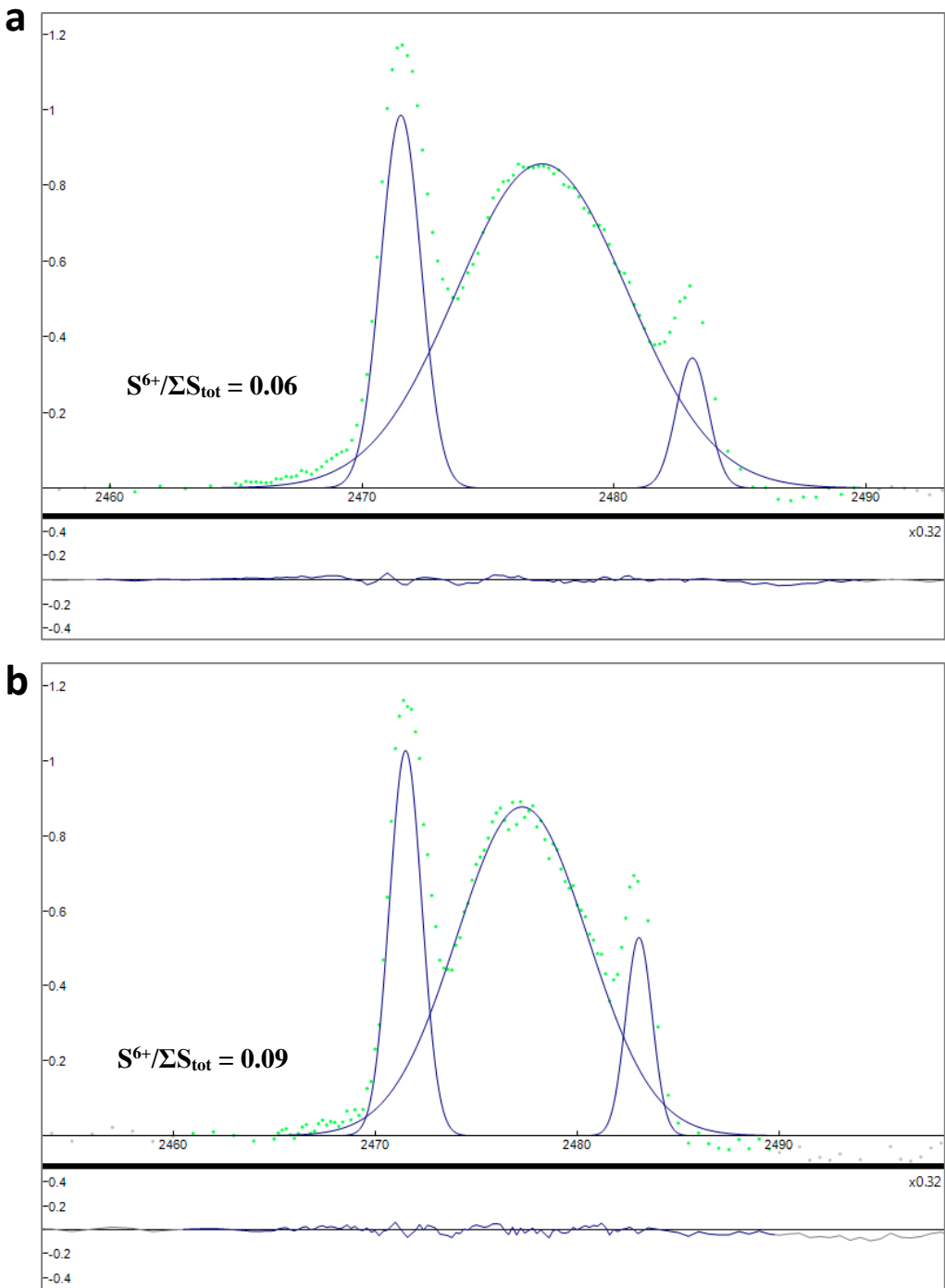
b.d. = below level of detection. * Average of the core and rim S isotope and S contents values for the zoned grain. [†] Same apatite grain measured in both January and May 2019.







Supplementary Figure 11. Typical Fityk peak-fitted S-XANES spectra of apatite in Apollo samples. **a**, 12039 Ap001_a; **b**, 15016 Ap42; **c**, 15058 Ap012a; **d**, 15065 Ap005b; **e**, 15475 Ap003b.



Supplementary Figure 12. Fityk peak-fitted S-XANES spectra of **a**, a pyroxene grain in Apollo sample 15058; **b**, symplectite glass in Apollo sample 15058. The spectra of **a**, and **b**, show different peak characteristics when compared with apatite Ap012a from the same (15058) Apollo sample (c.f. Supplementary Figure 11 C) above).

With the exception of sample 15016, a correlation between S abundance and S oxidation state ($S^{6+}/\Sigma S_{tot}$) was not observed (unlike for S isotopes (see main article)) for the apatites studied with S-XANES. For example, the apatites of samples 15016 and 15065 both contain high levels of S (Supplementary Table 2) and yet 15016 has an average $S^{6+}/\Sigma S_{tot}$ value of 0.55, whereas 15065 has average $S^{6+}/\Sigma S_{tot}$ values of 0.25 to 0.36. For terrestrial apatite high S abundances are positively

correlated with high oxygen fugacity ($f\text{O}_2$) (ref. ²²). When S-XANES analyses on a natural terrestrial apatite and an experimentally crystallised apatite were compared with their corresponding electron backscatter diffraction (EBSD) patterns⁴¹, the S oxidation state as a function of crystallographic orientation was found to vary, suggesting that there was evidence for the simultaneous incorporation of S^{6+} and S^{2-} at different crystallographic sites within the apatite (*T*-site and *X*-site, respectively). Thermodynamic modelling has also shown that S^{2-} might be stable in the *X*-site, with a prediction that S^{2-} resides closest to Cl^- in natural apatite⁴².

An explanation for the high S abundances, the lack of positive correlation with $f\text{O}_2$ and the dominance of S^{2-} (with the exception of sample 15016) for lunar apatites studied in this project, might be that S is situated within both the crystallographic *T*- and *X*-sites of apatite. Sample 15016 has high S contents and a higher S oxidation state which might suggest that S is predominantly situated within the *T*-site.

Oxidized melts are not expected because mare basalts and, therefore, the apatites crystallised within the rocks, are believed to have formed under reducing conditions in a low oxygen fugacity environment (IW-1 (e.g. refs. ⁸⁰⁻⁸²)). The reduced form of sulfur, S^{2-} , is expected to be the only oxidation state of sulfur to exist under such conditions (e.g. refs. ⁸³⁻⁸⁶). The current study has shown that the more oxidized state of S (S^{6+}) is present in every lunar apatite analysed and both S^{6+} and S^{2-} exist simultaneously in late-stage lunar silicate melts when apatite is a crystallising phase. It has recently been suggested²³ that S^{6+} could be present at very low levels (currently undetectable) in a reduced ($\leq\text{FMQ}$ redox buffer) silicate melt. Apatite will preferentially incorporate the more oxidized S^{6+} relative to S^{2-} into its crystallographic structure (the *T*-site)^{19,22,23} which means that even if S^{6+} is not abundant enough to be measured in a reduced silicate melt, it can be preferentially sequestered and, therefore, more easily detected in apatite²³.

The S-XANES analyses has complemented the NanoSIMS work by providing further evidence of which S species resided in the late-stage basaltic silicate melt from which apatite crystallised and, therefore, the S species that was degassed. A melt dominated by S^{2-} contained the reduced form of S, whereas a melt dominated by SO_4^{2-} contained the oxidized form of sulfur, S^{6+} . The three distinct S isotope groups can, therefore, be partially explained by variable levels of S degassing from reduced, oxidized or a combination of both reduced and oxidized late-stage silicate melts (Figure 3 main article).

Additional references

45. McGee, P., Warner, J. & Simonds, C. Introduction to the Apollo collections. Part 1: Lunar igneous rocks. Technical Report No. 77: 22034 (1977).
46. Beaty, D. W. & Albee, A. L. Comparative petrology and possible genetic relations among the Apollo 11 basalts. *Proc. 9th Lunar Planet. Sci.* **1**, 359-463 (1978).
47. Beaty, D. W., Hill, S. M. R., Albee, A. L. & Baldridge, W. S. Apollo 12 feldspathic basalts 12031, 12038 and 12072 - Petrology, comparison and interpretations. *Proc. 10th Lunar Planet. Sci.* **1**, 115-139 (1979).
48. Rhodes J. M., Blanchard D. P., Dungan M. A., Brannon J. C. & Rodgers K.V. Chemistry of Apollo 12 mare basalts: Magma types and fractionation processes. *Proc. 8th Lunar Planet. Sci.* **2**, 1305-1338 (1977).
49. Neal, C. R. et al. Basalt generation at the Apollo 12 site, Part 1: New data, classification, and re-evaluation. *Meteorit. Planet. Sci.* **29**, 334-348 (1994).
50. Nyquist, L. E., Shih C.-Y., Wooden, J. L., Bansal, B. M. & Wiesmann H. The Sr and Nd isotopic record of Apollo 12 basalts: Implications for lunar geochemical evolution. *Proc. 10th Lunar Planet. Sci.* **1**, 77-114 (1979).
51. Papike, J. J., Hodges, F. N., Bence, A. E., Cameron, N. & Rhodes, J. M. Mare basalts: Crystal chemistry, mineralogy, and petrology. *Rev. Geophys. Space Phys.* **14**, 475-540 (1976).
52. Taylor, L. A., Patchen, A., Mayne, R. G. & Taylor, D.-H. The most reduced rock from the moon, Apollo 14 basalt 14053: Its unique features and their origin. *Am. Mineral.* **89**, 1617-1624 (2004).
53. NASA *Lunar Sample Information Catalog Apollo 15*, 51-265 (1971).
54. Bence, A. E. & Papike, J. J. Pyroxenes as recorders of lunar basalt petrogenesis: chemical trends due to crystal-liquid interaction. *Proc. 3rd Lunar Planet. Sci.* **1**, 431-469 (1972).
55. Ryder, G. Catalog of Apollo 15 Rocks: Part 1. NASA, Curatorial Branch Publication 72, JSC no. 20787, 1-338 (1985).
56. Rhodes, J. M. & Hubbard, N. J. Chemistry, classification, and petrogenesis of Apollo 15 mare basalts. *Proc. 4th Lunar Planet. Sci.* **2**, 1127-1148 (1973).
57. Nava, D. F. Chemical compositions of some soils and rock types from the Apollo 15, 16 and 17 lunar sites. *Proc. 5th Lunar Planet. Sci.* **2**, 1087-1096 (1974).
58. Cuttita, R. et al. Chemistry of twenty-one igneous rocks and soils returned by the Apollo 15 mission. *Proc. 4th Lunar Planet. Sci.* **2**, 1081-1096 (1973).
59. NASA *Apollo 15 Preliminary Science Report*, 5-1 – 6-1 (1972).
60. Wieczorek, M. A. et al. in *Reviews in Mineralogy and Geochemistry: New Views of the Moon*, 60 (eds Jolliff, B. L., Wieczorek, M. A., Shearer, C. K. & Neal, C. R.) 221-364 (The Mineralogical Society of America, Virginia, 2006).
61. Nord, G. L. et al. Petrologic study of igneous and metaigneous rocks from Apollo 15 and 16 using high voltage transmission electron microscopy. *Proc. 4th Lunar Planet. Sci.* **1**, 953-970 (1973).

62. Ryder, G. Catalog of Apollo 15 Rocks: Part 3. NASA, Curatorial Branch Publication 72, JSC no. 20787, 779-1296 (1985).
63. Bickel, C. E., Warner, J. L. & Phinney, W. C. Petrology of 79215: Brecciation of a lunar cumulate. *Proc. 7th Lunar Planet. Sci.* **2**, 1793–1819 (1976).
64. McGee, J. J., Bence, A. E., Eichhorn, G. & Schaeffer, O. A. Feldspathic granulite 79215: Limitations on $T-fO_2$ conditions and time of metamorphism. *Proc. 9th Lunar Planet. Sci.* **1**, 743–772 (1978).
65. Ravel, B. & Newville, M. ATHENA, ARTEMIS, HEPHAESTUS: data analysis for X-ray absorption spectroscopy using IFEFFIT. *J. Synchrotron Radiat.* **12**, 537-541 (2005).
66. Jugó, P. J., Wilke, M. & Botcharnikov, R. E. Sulfur K-edge XANES analysis of natural and synthetic basaltic glasses: Implications for S speciation and S content as function of oxygen fugacity. *Geochim. Cosmochim. Acta* **74**, 5926–5938 (2010).
67. Wojdyr, M. Fityk: A general-purpose peak fitting program. *J. Appl. Cryst.* **43**, 1126–1128 (2010).
68. Potts, N. J., Barnes, J. J., Tartèse, R., Franchi, I. A. & Anand, M. Chlorine isotopic compositions of apatite in Apollo 14 rocks: Evidence for widespread vapor-phase metasomatism on the lunar nearside ~4 billion years ago. *Geochim. Cosmochim. Acta* **230**, 46–59 (2018).
69. Gibson, E. K. Jr. & Moore, G. W. Sulfur abundances and distributions in the valley of Taurus-Littrow: Evidence of mixing. *Proc. 5th Lunar Planet. Sci.* **2**, 1823–1837 (1974).
70. Kerridge, J. F., Kaplan, I. R. & Petrowski, C. Light element geochemistry of the Apollo 16 site. *Geochim. Cosmochim. Acta* **39**, 137-162 (1975).
71. Kerridge, J. F., Kaplan, I. R. & Petrowski, C. Evidence for meteoritic sulfur in the lunar regolith. *Proc. 6th Lunar Planet. Sci.* **2**, 2151-2162 (1975).
72. Bombardieri, D. J., Norman, M. D., Kamenetsky, V. S. & Danyushevsky, L. V. Major element and primary sulfur concentrations in Apollo 12 mare basalts: The view from melt inclusions. *Meteorit. Planet. Sci.* **40**, 679-693 (2005).
73. Hauri, E. H., Weinreich, T., Saal, A. E., Rutherford, M. C. & Van Orman, J. A. High pre-eruptive water contents preserved in lunar melt inclusions. *Science* **333**, 213-215 (2011).
74. Chen, Y. et al. Water, fluorine, and sulfur concentrations in the lunar mantle. *Earth Planet. Sci. Lett.* **427**, 37-46 (2015).
75. Ni, P., Zhang, Y., Chen, S. & Gagnon, J. A melt inclusion study on volatile abundances in the lunar mantle. *Geochim. Cosmochim. Acta* **249**, 17–41 (2019).
76. Boyce, J. W. et al. Lunar apatite with terrestrial volatile abundances. *Nature* **466**, 466-469 (2010).
77. Greenwood, J. P., Itoh, S., Sakamoto, N., Warren, P., Taylor, L., Yurimoto, H. Hydrogen isotope ratios in lunar rocks indicate delivery of cometary water to the Moon. *Nat. Geo.* **4**, 79-82 (2011).
78. Konecke, B. A., Fiege, A., Simon, A. C. & Holtz, F. Cryptic metasomatism during late-stage lunar magmatism implicated by sulfur in apatite. *Geology* **45**, 739-742 (2017).

79. Baker, D. R. & Moretti, R. in *Sulfur in Magmas and Melts: Its Importance for Natural and Technical Processes* (eds Behrens, H. & Webster, J. D.) 167-213 (Reviews in Mineralogy and Geochemistry 73, Mineralogical Society of America, 2011).
80. Sato M., Hickling N. L. & McLane J. E. Oxygen fugacity values of Apollo 12, 14, and 15 lunar samples and reduced state of lunar magmas. *Proc. 4th Lunar Planet. Sci.* **4**, 1061-1079 (1973).
81. Longhi, J. Experimental petrology and petrogenesis of mare volcanics. *Geochim. Cosmochim. Acta* **56**, 2235-2251 (1992).
82. Wadhwa, M. in *Reviews in Mineralogy and Geochemistry: Oxygen in the Solar System*, 68 (eds MacPherson, G. J.) 493-510 (The Mineralogical Society of America, Virginia 2008).
83. Fincham, C. J. B. & Richardson, F. D. The behaviour of sulphur in silicate and aluminatite melts. *Proc. R. Soc. A: Mathematic. Phys. Eng. Sci.* **223**, 40-62 (1954).
84. Carroll, M. R. & Rutherford, M. J. Sulfide and sulfate saturation in hydrous silicate melts. *J. Geophys. Res.* **90**, C601–C612 (1985).
85. Wallace, P. & Carmichael, I. S. E. Sulfur in basaltic magmas. *Geochim. Cosmochim. Acta* **56**, 1863-1874 (1992).
86. Wilke, M. et al. The origin of S⁴⁺ detected in silicate glasses by XANES. *Am. Mineral.* **93**, 235-240 (2008).